SAN02000-1154J

Phase structure within a fracture network beneath a surface pond: Field experiment

R.J. Glass[1] and M.J. Nicholl[2]

[1]Flow Visualization and Processes Laboratory

Sandia National Laboratories

Albuquerque, NM 87185-0735

email: rjglass@sandia.gov

[2]School of Geology

Oklahoma State University

Stillwater, OK 74078

email: nicholl@okstate.edu

DISCLAIMER

DISCLAIMER

Portions of this document may be illegible in electronic image products. Images are produced from the best available original document.

Abstract

We performed a simple experiment to elucidate phase structure within a pervasively fractured welded tuff. Dyed water was infiltrated from a surface pond over a 36 minute period while a geophysical array monitored the wetted region within vertical planes directly beneath. We then excavated the rock mass to a depth of ~5 m and mapped the fracture network and extent of dye staining in a series of horizontal pavements. Near the pond the network was fully stained. Below, the phase structure immediately expanded and with depth, the structure became fragmented and complicated exhibiting evidence of preferential flow, fingers, irregular wetting patterns, and varied behavior at fracture intersections. Limited transient geophysical data suggested that strong vertical pathways form first followed by increased horizontal expansion and connection within the network. These rapid pathways are also the first to drain. Estimates also suggest that our excavation captured from ~10% to 1% or less of the volume of rock interrogated by our infiltration slug and thus the penetration depth could have been quite large.

1. Introduction

In recent years, a significant body of research has considered flow and transport in unsaturated fractured rock within arid environments. Early conceptual models [e.g., Wang and Narasimhan, 1985; 1993; Pruess and Wang, 1987; Peters and Klavetter, 1988] have been called into question by both laboratory experiments focused on basic processes [e.g., Glass et al., 1995, 1996; Tokunaga and Wan, 1997] and field evidence that indicates rapid deep percolation in arid environments [e.g., Russell et al., 1987; Fabryka-Martin et al., 1996; Yang et al., 1996; Davidson et al., 1998]. Calculational models have been proposed to fix some of these conceptual model failures; however, such models typically rely on calibrated approaches, and hence are unable to provide better understanding of system behavior [e.g., Liu et al., 1998]. While laboratory experiments greatly increase our fundamental understanding of physical processes, field experiments contain a much higher level of ambiguity, as measurements are difficult to make and interpret [e.g., Kilbury et al., 1986; Drier et al., 1987; Gimmi et al., 1997; Bussod et al., 1999; Faybishenko et al., 1999].

Conceptualization of transport within an unsaturated fractured rock mass requires an understanding of the evolving geometry, or structure, of the water/air phases. In addition to defining transport pathways for water and solutes, this structure also sets the domain for interactions between the phases (air/liquid/solid). Full treatment of this problem requires that we consider phase structure within the entire void space (fracture and matrix). At one end of the spectrum, fractures merge with the matrix and become indistinguishable; at the other end, the matrix becomes negligible relative to the fractures. Here, we constrain ourselves to the end member of a fracture network within an impermeable rock matrix.

While very little experimental data exists for unsaturated flow in fracture networks, research in single fractures has been reviewed in the context of two-phase flow [National Research Council, 1996]. Under low flow conditions, where viscous forces are small relative to capillary or gravity forces, laboratory experiments and numerical simulations have shown highly complicated structures to form in single fractures. These structures include gravity driven fingers, phase entrapment within individual fractures, and intermittent/chaotic dripping. In each case, phase structure may span the fracture in at least one direction while wetting only a small portion of the fracture surfaces. At higher flow rates, viscous forces increase, capillary/gravity induced complication decreases, and structure of the wetting phase within the fracture becomes more pervasive. More recently, it has also been found that under certain pressure regimes, non-aperture spanning water film flow within the roughness of the rock surfaces can define an additional conductive structure [e.g., Tokunaga and Wan, 1997; Or et al., 1999].

In addition to physical properties of the fracture network, accessibility to the infiltrating phase will combine with capillary, gravity, and viscous forces to determine phase structure. We categorize network properties into: 1) spatial distribution of individual fracture properties, e.g., each fracture will differ in terms of aperture statistics (mean, variance, spatial correlation), spatial extent, 3-D topology, and inclination; 2) network topology or fracture connectivity; and 3) the properties of the individual fracture connections which may form a network within the network. While there is no data to suggest how individual fracture properties might vary within a network, a significant body of research has considered network topology in the context of geomechanics and saturated flow [e.g., Renshaw, 1996; Margolin et al., 1998]. With regard to intersections between individual fractures, physical characteristics and behavior under unsaturated flow conditions are unknown, and may play a critical controlling role in determining phase structure within the network. If we consider the simplest geometry of an expanded cross, an intersection will

create a capillary barrier that is more difficult for the wetting phase to invade, and therefore, has the potential to compartmentalize (break up) capillary dominated flow structure. Functioning as capillary barriers [Glass et al., 1995, 1996], such intersections would work to both concentrate flow at the scale of an individual fracture (i.e., cause the confluence of gravity driven fingers above an intersection), and fragment flow at the network scale (i.e., break lateral connection via vertical barriers). By analogy to behavior in single fractures, increased viscous forces are expected to decrease capillary/gravity induced complication, and produce a more pervasive flow structure that is primarily controlled by heterogeneous permeability within the viscous field. Under these conditions, fracture intersections may provide connected high flow pathways, instead of restricting phase invasion.

To appropriately consider phase structure within fracture networks, experiments are required where we can systematically vary the relative importance of capillary, gravity and viscous forces within a controlled fracture network topology. In the formative stages of such an effort, guidance from field experiments is highly desirable, even though interpretation and generalization of results is always difficult. In 1994, an opportunity arose to conduct a simple field experiment that would explore flow structure in an initially dry fracture network under a surface pond. Construction of a test facility at the Nevada Test Site (NTS) required the excavation of a large, pervasively fractured rock mass having hydraulic properties that precluded significant matrix interaction. We infiltrated a water slug containing a visible tracer into the rock unit and attempted to follow evolution of the structure with a geophysical array. Then, during subsequent excavation, we mapped the fracture network and tracer distribution within a series of horizontal pavements immediately below the infiltration surface. For the simple situation of ponded infiltration, we expected a transition from full participation of the network near the pond (saturated conditions prevalent), to partial participation further away as pressures move into tension and unsaturated flow processes dominate. As flow transitions into unsaturated conditions,

capillary heterogeneity, gravity, and the role of fracture intersections should show themselves to fragment the phase structure and create complication both within the network, and individual fractures. We present and interpret the results of our experiment here. To our knowledge, no investigation of this type has ever been performed in an intact rock unit. Thus our study yields a first-order description of system behavior to be used as a basis for designing subsequent laboratory and field investigations.

2. Experimental Investigation

Our experiment was performed adjunct to construction activities associated with the Large Block Test (LBT), a scientific investigation conducted by Lawrence Livermore National Laboratory (LLNL) on the eastern slope of Fran Ridge near Yucca Mountain, Nevada [see Lin et al., 1994; Wilder et al., 1997]. Design for the LBT called for careful exhumation of a test block (4.5 x 3 x 3 m) from a surface outcrop of nonlithophysal Topopah Spring tuff; a stratigraphic unit being considered as a potential host for disposal of high-level radioactive waste. Excavation activities began with the creation of a level work area (~12 x 12 m) at a depth of 1-3 m below surface (figure 1); the LBT block was then isolated from the formation with vertical saw cuts.

A ~6 m^2 (8 x 8') location in the southwest corner of the leveled area was selected for our infiltration test (figure 1). Visual inspection of the pavement and excavation walls suggested that the extremely tight matrix would confine flow to the pervasive (< 30 cm spacing) fracture network. Because potential evapotranspiration in this region (125-200+ cm/year) greatly exceeds annual rainfall (8-10 cm/year) [Bedinger et al., 1990], dry initial conditions were expected for the near surface fracture network. Following site selection, a shallow (~0.2 m) infiltration basin (~3.5 m^2 surface area) was excavated into the rock surface. A geophysical array was also installed (see below) to test the utility of electrical

resistance tomography (ERT) for detecting water content changes within the network. Local well water was used as the infiltrating fluid; blue food coloring (FD&C Blue #1) was added (~4 g/l) as a visible tracer consistent with environmental mandates. The test was initiated by pouring ~150 liters of fluid into the basin from buckets. At the same time, gravity flow was induced from a tank located several meters above the infiltration basin; a float valve controlled fluid level in the basin. Fluid level in the feed tank was monitored at 10 second intervals with a pair of pressure transducers. Metered flow from the feed tank (~640 liters) ended after ~36 minutes, for a total infiltration volume of ~790 liters.

Approximately eight weeks after conclusion of infiltration, waste rock surrounding the LBT block (including the region of our test) was removed in a series of roughly horizontal lifts. At each level, the exposed rock pavement was broken to a depth of ~0.5 m with a large vehicle-mounted jackhammer (~0.5 m chisel) and most of the waste rock was removed with a small bulldozer. The pavement was then cleaned to bare rock over a ~6 m^2 (8 x 8') area directly below the infiltration site. Large rocks were moved by hand, and fine debris was blown away with pressurized air. The fracture network and tracer distributions were mapped at the infiltration surface (level 0), and at each of the eleven subsequent excavation levels (1-11). Maps were referenced to a portable 2.44 x 2.44 m (8 x 8') grid that was subdivided at 0.305 x 0.305 m (1 x 1') intervals. Fracture traces and dye stains were recorded at a scale of 1" = 1' by hand mapping. The longest fracture traces were mapped first, and then successively smaller features as time allowed. Wherever possible, the dip of individual fractures was measured (+/- 5°) on exposed surfaces. During excavation, we also noted the approximate location and extent of tracer encountered outside of the mapped area on the excavation walls, and in the excavated rubble.

The excavation process was designed specifically for the LLNL investigation, placing some constraints on our mapping process. 1) Interval between pavements was not consistent. 2)

Roughness and dip of the mapped area varied considerably. 3) Only a small area was cleared to bare rock, hence we were unable to obtain a detailed record of tracer migration outside of the mapped area. 4) Excavation was restricted to horizontal pavements; therefore we could not explore evidence of flow mechanisms in the plane of inclined fractures (e.g., gravity driven fingering) except through observation of broken blocks. 5) Time constraints were imposed by the excavation schedule; mapping activities were performed immediately after a lift was cleaned, and in the shortest possible time. As a result, maps taken at levels 7, 9, and 10 contain less detail than those at other levels. 6) Excavation stopped at a depth of ~5 m, while the infiltration pulse clearly penetrated below this depth.

Investigators from LLNL used Electrical Resistance Tomography (ERT) to map resistivity of the rock in a set of two-dimensional vertical planes beneath the infiltration basin. Test design was to bring flow to steady-state, and then image fluid within the instrumented prism. Data was collected before, during, and after infiltration using electrode strings installed within the basin at the corners of a square (1.5 m on a side); orientation was chosen to provide maximize coverage across the primary vertical fracture sets. Each 3 m long ERT probe contained 11 electrodes (30 cm apart) and was grouted into a dry drilled vertical hole. Installation was designed to minimize perturbations to the system, provide electrical contact with the rock mass, and inhibit the formation of preferential pathways. Eight shallow (~15 cm) surface electrodes were installed along diagonals of the square to increase resolution in those planes. Infiltration rate was much higher than expected; hence measurements during infiltration were limited to two sequential cross-hole ERT resistance fields in one plane (strings 1 and 3). Fields between all string pairs were measured over the hour following infiltration, and on the next day.

3. Results and Interpretation

Following infiltration, data was collected in the form of pavement maps, 35 mm slides of the excavation, and visual observations. Fracture traces at each excavation level are shown in figure 2; gray regions on the maps denote zones where dyed fractures were found. The pavement maps clearly delineate fracture traces and distribution of tracer within the ~6 m^2 mapped region directly beneath the infiltration surface (figure 3). Outside that region, we have estimated lateral extent of the tracer from the remaining data (35 mm slides and visual observations). This was an imperfect process, as the surrounding pavement was mostly covered in rubble and varied significantly in elevation. Because of the limitations on this data, we have simply outlined areas in which dye was found, and not attempted to depict structure within those areas. The phase structure clearly spread beyond the region of detailed mapping to produce an irregular structure that occupied ~35 m^3 of the excavated rock mass and obviously extended below the 5 m depth of excavation. Within the dyed zone, complication of the dye structure varied from pervasive stain near the infiltration surface to more fragmented structures at depths of 2-5 m. In the following, we first consider our map data to describe in detail the fracture network geometry and dye tracer structure. ERT results are then presented followed by estimates for the mean hydraulic aperture for the fractures adjacent to the pond and the total volume of rock that the test may have interrogated. Based on these results, we end this section with a suggestion for a future experiment.

3.1 Fracture network geometry:

Pavement maps (figure 2) yielded measurements of trace length for 741 fractures, and orientation (dip/dip direction) for 572 fractures. Dip measurements were not recorded in the field if neither fracture surface was exposed (~23% of all fractures), which was most likely

to occur for small aperture, near-vertical fractures. Measured fracture orientations (figure 4) exhibited two strong near-vertical sets; one trending to the NW/SE, and the other to the SW/NE. The extensive near-vertical fractures (> 2 m trace length) appeared to maintain a consistent orientation with depth, and exhibited less variability than did the smaller features. Throckmorton et al. [1995] measured two test pits (~4-5 m deep) and pavement areas immediately (several meters) south and west of our experiment (figure 1). In the location closest to our experiment (TOB1), they reported two sets of steeply dipping cooling joints, and two younger sets of steeply dipping tectonic joints; reported orientations for those sets are consistent with our measurements (figure 4). Fracture trace lengths commonly display an exponential distribution, with the probability of occurrence (p) for a specific trace length (L) given by $p = e^{-CL}$ [Call et al., 1976]. Approximately 60% of the measured fractures at our site extended past the boundaries of the mapped area. The remaining 40% exhibited an exponential distribution, with C = ~1.7. The presence of extensive fractures at this locality is supported by data of Throckmorton et al. [1995] that report truncated trace lengths of up to 10 m.

Horizontal pavements preferentially sample steeply dipping fractures, and under sample those with a shallow dip (subhorizontal). Furthermore, the excavation method tended to damage and fragment the surface of subhorizontal features. As a result, our measured data (figure 4) includes few examples of such features. However, we did note subhorizontal fractures at most excavation levels, particularly at shallower depths. Numerous subhorizontal fractures were also observed in the excavation walls. Available data suggested that these undulating fractures dipped slightly in the general direction of the topography (north and east). This observation is consistent with data measured in the adjacent pit by Throckmorton et al. [1995]. They reported two sets of subhorizontal fractures; one dipping ~10° to the SE, and the other ~5° to the NE; the first set was attributed to cooling, and the second to erosional unloading. They also report fracture

spacings on the order of 0.3 - 1 m, with localized zones spaced on the order of 5 cm. Again, their reported data is consistent with our observations.

The excavation method did not allow us to explicitly follow individual fractures in the vertical direction; however, we were able to identify a number of features that are obviously connected between mapping levels. In particular, all pavement maps (figure 2) show an extensive fracture (marked on the figures with a black square) beginning slightly north of the SW corner and trending towards the NE corner. In some maps, this fracture appears to be broken into segments; an observation that we believe to be an artifact of surface roughness in the mapped region. Relatively long, near vertical fractures trending to the NNW are prevalent along the western side of the mapped area, which appears to be more densely fractured than the eastern side. The maps also show strong connectivity in the horizontal plane. In the excavation walls, steeply-dipping fractures were observed to extend from the soil zone down through the bottom of the excavation, a distance of greater than 6 m. Nearby, Throckmorton et al. [1995] reported fracture heights as great as 12 m, and truncated lengths of 6-10 m. We observed truncated subhorizontal features with trace lengths on the order of 2 m, and Throckmorton et al. [1995] reported lengths of 5+ m. The presence of such pervasive and extensive fractures points to a very well connected network, in both the vertical and horizontal directions. Finally, multiple episodes of fracturing [Throckmorton et al., 1995] from a variety of mechanisms (cooling, tectonic, unloading) will also have enhanced connectivity, as later fractures are expected to terminate in the earlier ones.

3.2 Dye tracer structure:

At each excavation level, spatial extent of the flow field was estimated by combining data from the pavement maps with observations made during excavation (figure 2). With

increasing depth, estimated extent of the flow field first expands and then contracts (figure 5). At the infiltration surface, dye was only observed within the surface pond. However, at the first level below the infiltration surface, dye was observed both inside (all but the SW corner) and outside (to the north and east) of the mapped area. Over the next intervals, the stained area alternatively expanded and contracted with depth in all directions except SW, which remained tracer free throughout the depth of excavation. A persistent near-vertical fracture crossing the SW corner of the mapped area appeared to form a barrier that separated stained and unstained regions.

At depths of ~1-4 m (levels 3-8), the dyed structure appeared to expand as several disjoint appendages. The surface of a vertical fracture exposed in the south wall of the excavation was partially (~0.2 - 0.5 m^2) stained (figure 6). While this fracture did not pass through the mapped region, it clearly connected with two near-vertical fractures that did. A persistent SW-NE trending fracture that dissected the mapped area (described above) clearly showed dye stain NE of the mapped area (figure 7). In that direction, small dye stains were observed ~2-3 m NE of our mapped area in near-vertical fractures exposed along the face of a 1 m buffer zone surrounding the LBT block. We also noted a subhorizontal fracture exposed in the south wall of the excavation (level 7) that showed stain over a ~1.5 m long portion of its length. At level 8, pavement extending to the N and NW of the mapped area showed heavy stain, as did rubbelized rock excavated 3-4 m to the north. At level 10, dye stain was noted in the south wall of the excavation ~ 3m east of our mapped area. By the bottom of the excavation (level 11), all but one of these appendages appeared to have died out, and in the final three levels (9-11), the stained region contracted to approximately the same area as the original pond.

The pavement maps provide a representative and detailed record of tracer distribution within the ~30 m^3 prism directly below the infiltration surface. Immediately (< 1 m) below

the infiltration basin, all mapped fractures except those in the extreme SW corner of the mapped region were completely stained, including the few exposures of subhorizontal features that were undamaged by excavation. At greater depth (~2-3 m and below), distribution of tracer within the mapped region became complicated and fragmented (figure 3). Many fractures were not stained, and others only partially so, often despite obvious physical connection to stained portions of the network. On some long, near-vertical fractures, stain was restricted to portions of the fracture trace, yielding alternating bands of stained and unstained regions. Complicated tracer patterns were observed on a number of fracture surfaces pulled from the rubble; figure 8 shows a pattern in which the tracer appears to surround unstained regions, while the tracer seen in figure 9 appears to span the fracture surface in only one direction.

Laboratory and numerical investigations of fluid invasion along the plane of a horizontal fracture [Glass et al., 1998] have shown that slow displacement of a non-wetting fluid by a wetting fluid can lead to the formation of complicated invasion fronts and significant air entrapment such as that seen in figure 8. As compared to a fully saturated fracture, the wetted structure implied from figure 8, would produce a reduced satiated permeability [Nicholl et al., 2000] in the horizontal direction, restrict passage of fluid through adjacent matrix blocks, and afford smaller contact area for imbibition into the adjacent matrix [Glass et al., 1995, 1996]. In non-horizontal fractures, a number of studies have considered the formation of gravity-driven fingers where flux drops below the product of saturated conductivity of the fracture and the gravitational gradient [e.g., Nicholl et al., 1992; 1993a,b; 1994; Glass 1993; Su et al., 1999]. This condition is expected to occur within the fragmented field away from the ponded source. While we found numerous instances where the pavement was stained along short (2-10 cm) lengths of a fracture (figure 3), and figure 9 is more likely a gravity-driven finger than an image of the rare blue rock scorpion, we can

not conclusively differentiate these observations from capillary driven flow through small apertures.

Finally, we emphasize the wide variety of tracer configurations found at fracture intersections (e.g., figure 3). In some instances, both fractures were fully stained. We also observed situations where one fracture was fully stained in the vicinity of the intersection, while the other fracture showed no evidence of tracer, or tracer was seen to extend only a short distance (~2-15 cm) away from the intersection. Occasionally, small spots of tracer were observed on subhorizontal fractures. On closer inspection, it was discovered that these locations corresponded to intersections between vertical hairline fractures. The excavation method did not expose the surfaces of many vertical fractures; however, some showed dark tracer stains along the lower edge that faded in color upward before disappearing. The rock ledge shown in figure 10 is a rare instance where the rock broke in a manner that allowed us to see the face of a vertical fracture with stains suggesting the fracture below to have formed a capillary barrier that possibly concentrated flow.

3.3 ERT results:

Our test design incorporated ERT in the hope that we would be able to map the phase structure development to steady state beneath the surface pond. Additionally, correlation to maps of both fractures and flowing fractures would allow an assessment of the method in fracture networks. Unfortunately, because of Yucca Mountain Project constraints and budget limitations, data was only reduced in a preliminary fashion, as can be found in archived scientific notebooks (LLNL YMP controlled scientific notebook LBT-03, 3/4/94, pp. 5-26). Application of a standard inversion algorithm led to two-dimensional images that clearly show changes in electrical resistivity within the instrumented prism. Because of the influence of water on the bulk dielectric, decreases in resistivities constitute increases in

moisture content; the larger the resistivity decrease, the higher the water saturation in the region.

Images of the plane between strings 1 and 3 were constructed at 9, 36 (when water addition stopped), 77, and 1320 minutes following infiltration (note that each of these times constitutes an average over the previous ~10-20 minutes). By 9 minutes, water had completely traversed the 3 m depth, with a high saturation region directly beneath the pond (~30 cm) and two high saturation pathways, one near each side of the plane (30-40 cm wide) which connected near the bottom. Approximately 40% of the plane showed no increase in water content above initial. At 36 minutes, the high saturation region beneath the pond had extended to ~45 cm and one of the pathways had increased in saturation, however, ~30% of the plane remained at initial saturation. At 77 minutes, most regions which showed high saturation at 7 and 36 minutes had desaturated to near initial levels while the large zone in the middle of the plane that had been at initial levels has increased in saturation, presumably due to slow lateral flow within the fracture network. By 1320 minutes, most of the field has reduced to near initial contents except for the middle of the plane which continued to show increased saturation levels.

Images formed between all string pairs following infiltration show similar structures with depth and a significant decrease to near initial moisture content by the following day. While for the most part, zones of increased saturation have strong vertical and some horizontal connection, in some cases, they appear disconnected. Considering the transient data from the 1-3 plane as representative, ERT results suggest that strong vertical pathways may form first within the network followed by increased horizontal expansion and connection.

3.4 Estimation of mean hydraulic aperture:

Once the surface pond was established, infiltration rate (0.26 l/s) remained constant within the error associated with maintaining the pond. Assuming saturated vertical flow under unit gradient through fractures of length, L, in which the local conductivity is K_{sat}, Darcy's Law for flow across the infiltration surface can be written as:

$$Q = K_{sat}\langle b \rangle L \qquad \text{(eq. 1)}$$

where Q is the volumetric flow rate and <b> is the mean fracture aperture. As <b> is typically unknown, it is common to express the product of <b> and K_{sat} as the fracture transmissivity (T). Assuming that the fractures can be approximated by parallel plates gives:

$$T = \frac{b_h^3 g}{12\upsilon} \qquad \text{(eq. 2)}$$

where υ is kinematic viscosity of the fluid, and b_h is an effective hydraulic fracture aperture. Except in unusual (and perhaps pathologic) cases, b_h will be smaller than <b>. Combining eq. 1 and eq. 2 gives:

$$b_h^3 = \frac{12Q\upsilon}{gL} \qquad \text{(eq. 3)}$$

Measured length of fractures in the infiltration basin totaled ~33 m; kinematic viscosity of pure water at 25° C was taken from standard tables, giving b_h = 0.02 cm. We estimate that experimental uncertainty in flow rate, fracture length, fluid viscosity, etc., can affect b_h by

less than ~10%. However, since flow varies with the cube of b_h, the occurrence of connected large aperture regions within the fracture network can strongly influence our estimation of b_h, and thus it must be considered as an effective average over the area of the surface pond.

3.5 Possible rock volume interrogated by the flow field:

Discarding data from maps that were rushed to avoid interference with construction activity (7,9,10), we obtain an estimate for vertical volumetric fracture density of ~10 m^2/m^3. Data from Throckmorton et al. [1995] and observation of the excavation walls suggest that volumetric density for the subhorizontal fractures was on the order of ~ 2 m^2/m^3. By assuming that b_h provides a first-order estimate of <b>, we can estimate fracture porosity (~2.4 x 10^{-3}). This result implies that one liter of fluid would fully saturate the fracture network within ~0.4 m^3 of rock, and the total amount of fluid infiltrated (~790 liters) would have saturated the fractures in ~330 m^3 of rock. A number of factors would act to decrease this estimated volume: b_h is necessarily smaller that <b> and some fluid would be lost to matrix imbibition and numerous unmapped small aperture fractures. However, factors that would act to increase the estimated volume of rock affected by the fluid slug are much more significant: bypassed fractures, small-scale flow processes that lead to partial saturation (see above), and probable trends to decreasing fracture aperture and/or density with depth below the excavation.

As clearly evidenced from the ERT results, the fluid slug does not stop advancing when fluid in the pond is exhausted. Thus water draining from near-surface fractures will continue to supply the advancing infiltration front and allow its further penetration of the network. As flow rate through the network decreases in time, the wetting front becomes further destabilized. Increased instability will further fragment the invading phase,

producing fingers that narrow with depth. Eventually, individual fingers at the front will stop, and become pinned within the network. The formation of 'pools' above intersection induced capillary barriers, horizontal fractures, and film flow within the fractures will all work to bleed off fluid from advancing fingers. Within this drained structure, the residual moisture content will be much less than full saturation, an approximation of 0.2 being a reasonable estimate. Considering all of these, it is easy to envision a wetted rock mass that is one to even two orders of magnitude greater than the saturated estimate. We note that all of these estimates suggest that our excavation revealed only from ~10% to 1% or less of the total volume of rock that the experiment could have traversed. With these seemingly reasonable assumptions, water from our slug may have eventually penetrated to a depth of more than 100 m, a significant depth considering the short duration of the ponded source.

3.6 A suggested field experiment:

The ponded infiltration test presented here produced a final phase structure that varied from pervasive to complex. Unfortunately, a single test such as this cannot evaluate the competing influences of capillary, gravity, and viscous forces within the fracture network. In order to explore this competition, multiple experiments within a single fracture network must be performed. In context of the experiment presented here, one could use a series of highly adsorbed and distinguishable, visible tracers, each associated with a infiltration experiment where the imposed flow rate is systematically lowered from the ponded value. Between infiltration experiments, the network would be dried out to yield the same initial condition, possibly with the aid of forced air flow between boreholes installed at the site. ERT imagery would be used to follow each test followed by the complete and careful disassembly of the network using methods that would allow the best possible mapping of the network and tracer structures.

While circumstances prevented us from performing such a test, we did attempt two additional experiments to consider imposed infiltration rate in the northwest and northeast corners of the excavation surrounding the LBT (figure 1). In the northeast corner, we designed a restricted flow test in which fine sand tamped into the basin was expected to restrict flow into the network. This test failed during infiltration, when flow short-circuited the pond through a shallow subhorizontal fracture and rapidly appeared elsewhere at the ground surface. In the northwest corner, a small fluid slug (~20 liters) was applied to the network. Unfortunately, infiltration rate was dramatically lower due to the presence of caliche within the network. Although these two tests were located within 15 m of our primary test, material properties differed sufficiently to preclude direct comparison. This observation points out both the difficulty in planning such field tests and the degree of heterogeneity that may be encountered in unsaturated, fractured rock, especially near surface where significant weathering can occur.

4. Concluding Remarks

The phase structure observed beneath the surface pond in our experiment was generally consistent with our a priori expectations. Near the pond, where invasion rate and pressures are high and connection to the source complete, the network was fully stained. The phase structure immediately expanded beneath the pond; with depth, the structure became fragmented and complicated. Variability in the large scale lateral extent of the flow field is expected from the inherent variability of individual fractures within the network, and their connectivity. Additionally, fragmentation and complication are expected away from the pond as viscous forces decrease relative to capillary and gravity forces. We saw evidence of preferential flow, fingers, irregular wetting patterns, and varied behavior at fracture intersections; all of which have implications with respect to flow/transport in unsaturated fractured rock and the design of future experiments.

While our single experiment can not rigorously test hypothesized system behavior, it has given us an enhanced appreciation of both the complexity of unsaturated flow in a fracture network and the possible depths that water could reach from short periods of ponded infiltration. Under natural conditions, we expect that the topographic confluence of surface water at the upland beginnings of washes in arid environments such as Yucca Mountain will cause surface ponding at durations similar to what we imposed in our test. However, far from the infiltration surface we expect capillary and gravity forces to dominate, such as discussed by Glass et al. [1995, 1996].

We recognize a number of limitations in our measurements that affected our ability to characterize the fracture network, phase structure of the flow field, and temporal evolution of the system. However, despite these limitations, our data set provides a first glimpse into flow structure in an unsaturated natural fracture network. A simple modeling study based on this data has been reported by Eaton et al. [1996a,b] where both dual-permeability (DP) and equivalent-continuum (EC) approaches were applied. As one might expect, the two approaches resulted in strikingly different fluid distributions. And of course, neither displayed the rich variety of behavior observed in the field. Further modeling with increased complication, i.e., discrete fracture approaches, would yield a next iteration, and the incorporation of more heterogeneity could yield a closer correspondence to experiment. However, such a study must be carefully designed so that understanding is increased beyond simple 'heterogeneity calibration;' we must remember that all such simulation is constrained by assumptions in the underlying conceptual model and limitations resulting from the numerical implementation.

Our observations raise issues concerning the design of field experiments in unsaturated fractured rock that will yield increased fundamental understanding. The variable and

complicated nature of our flow structure implies a need for such detailed and extensive spatial coverage that installation of point-sensing devices would necessarily disrupt the natural system. Conversely, geophysical techniques that give spatial or temporal averages may not detect, or may misrepresent a complicated and evolving flow structure. Thus, unless the system is disassembled such as we have done, one may never know the full extent of the flow.

Acknowledgments

This field experiment was designed and data was collected with support from the U.S. Department of Energy, Office of Civilian Radioactive Waste Management, Yucca Mountain Site Characterization Project Office, under contract DE-AC04-94AL85000, WBS 1.2.5.4.6, WA-0040 and WA-0152, and QAGR 1.2.5.4.6 Revision 0; and is contained in SNL YMP controlled scientific notebooks entitled "Infiltration/Flow Path Visualization Test at Fran Ridge (parts 1 and 2)," YMP accession #'s MOL.19961029.0104 and MOL.19961029.0110, respectively. Analysis and interpretation of this data was supported by the U.S. Department of Energy, Basic Energy Sciences Geoscience Research Program under contract numbers DE-AC04-94AL85000 (Sandia National Laboratories) and DE-FG03-99ER14944 (Oklahoma State University). ERT imagery was designed and executed by B. Daily and A. Ramirez of LLNL. Mapping assistance was provided by D. Engstrom and S. McKenna of SNL. C. Rautman (SNL) provided invaluable assistance regarding the general geology of Yucca mountain. This work could not have occurred without the assistance of W. Lin and M. Owens of LLNL.

References

Bedinger, M.S., K.A. Sargent, and W.H. Langer, Studies of geology and hydrology in the basin and range province, southwestern United States, for isolation of high-level radioactive waste - Evaluation of the regions, USGS Professional Paper 1370-H, 61 p., 1990.

Bussod, G.Y., H.J. Turin, and B.A. Robinson, Unsaturated zone tracer testing at Busted Butte, Nevada: Phase 1 results and model predictions, 1999 Annual Meeting of the Geological Society of Am., Denver, CO, GSA Abstracts with programs, 31(7), A-491, 1999.

Call, R.D., J.P. Savely, and D.E. Nicholas, Estimation of joint set characteristics from surface mapping data, Proc. 17th US Symposium on Rock Mechanics, compiled by W.S. Brown, S.J. Green, and W.A. Hustrulid, pp. 2 B2-1-9, Snowbird, Utah, August 25-27, 1976.

Davidson, G.R., R.L. Bassett, E.L. Hardin, and D.L. Thompson, Geochemical evidence of preferential flow of water through fractures in unsaturated tuff, Apache Leap, Applied Geochemistry, 13, pp. 185-195, 1998.

Drier, R.B., D.K. Solomon, and C.M. Beaudoin, Fracture characterization in the unsaturated zone of a shallow land burial facility, in Flow and Transport Through Unsaturated Fractured Rock, D.D. Evans and T.J. Nicholson, editors, Geophysical Monograph 42, American Geophysical Union, Washington, D.C., 51-59, 1987.

Eaton, R.R., C.K. Ho, R.J. Glass, M.J. Nicholl, and B. W. Arnold, Modeling of flow through fractured tuff at Fran Ridge, Proc. 7th Int. Conf. of High Level Rad. Waste Manage., American Nuclear Society, April 29 - May 3, Las Vegas, NV, pp. 76-78, 1996a.

Eaton, R.R., C.K. Ho, R.J. Glass, M.J. Nicholl, and B.W. Arnold, Three-dimensional modeling of flow through fractured tuff at Fran Ridge, Sandia National Laboratories, Albuquerque, NM, SAND95-1896, 60 pp., 1996b.

Fabryka-Martin, J.T., P.R. Dixon, S.S. Levy, B. Liu, D.L. Brenner, L.E. Wolfsberg, H.J. Turin, and P. Sharma, Implications of environmental isotopes for flow and transport in the unsaturated zone at Yucca Mountain, Nevada, 1996 Annual Meeting of the Geological Society of Am., October 28-31, Denver, CO, GSA Abstracts with programs, 28(7), A-416, 1996.

Faybishenko, B., C. Doughty, S. Steiger, J. Long, T. Wood, J. Jacobsen, J. Lore, and P. Zawislanski. Conceptual model of the geometry and physics of water flow in a fractured basalt vadose zone: Box Canyon site, Idaho, LBNL Report 42925, 1999. (This is currently in review at Water Resources Research)

Gimmi, T., M Schneebeli, H. Fluhler, H. Wydler, and T. Baer, Field-scale transport in unsaturated crystalline rock, Water Resources Research, 33(4), pp. 589-598, 1997.

Glass, R.J., Modeling gravity driven fingering in rough-walled fractures using modified percolation theory, Proc. 4th Int. Conf. of High Level Rad. Waste Manage., American Nuclear Society, April 26-30, Las Vegas, NV, pp. 2042-2053, 1993.

Glass, R.J., M.J. Nicholl, and V.C. Tidwell, Challenging models for flow in unsaturated, fractured rock through exploration of small scale flow processes, Geophysical Research Letters, 22(11), 1457-60, 1995.

Glass, R.J., M.J. Nicholl, M.J., and V.C. Tidwell, Challenging and improving conceptual models for isothermal flow in unsaturated, fractured rock through exploration of small scale processes, Sandia National Laboratories, Albuquerque, NM, SAND95-1824, 61 pp., 1996.

Glass, R.J., M.J. Nicholl, and L. Yarrington, A modified invasion percolation model for low capillary number immiscible displacements in horizontal rough walled fractures: Influence of local in-plane curvature, Water Resources Research, 34(12), 3215-3234, 1998.

Kilbury, R.K., T.C. Rasmussen, D.D. Evans, and A.W. Warrick, Water and air intake of surface-exposed rock fractures in situ, Water resources Research, 22(10), pp. 1431-1443, 1986.

Lin, W., D.G. Wilder, J.A. Blink, S.C. Blair, T.A. Buscheck, D.A. Chesnut, W.E. Glassley, K. Lee, and J.J. Roberts, The testing of thermal-mechanical-hydrological-chemical processes using a large block, Proc. of the Fifth Ann. Int. Conf. on High Level Rad. Waste Mgmt., 1938-1945, Am. Nuclear Soc., Las Vegas, Nevada, May 22-26, 1994.

Liu, H.H., C. Doughty, and G.S. Bodvarsson, An active fracture model for unsaturated flow and transport in fractured rocks, Water Resources Research, 34(10), 2633-46, 1998.

Margolin, G., B. Berkowitz, and H. Scher, Structure, flow, and generalized conductivity scaling in fracture networks, Water Resources Research 34(9), 2103-2121, 1998.

National Research Counsel, Rock Fractures and Fluid Flow: Contemporary Understanding and Application, Committee on Fracture Characterization and Fluid Flow, National Academy Press, Washington, D.C., 1996.

Nicholl, M.J., R.J. Glass, and H.A. Nguyen, Gravity-driven fingering in unsaturated fractures, Proc. of the Third Ann. Int. Conf. on High Level Rad. Waste Mgmt., 321-331, Am. Nuclear Soc., Las Vegas, Nevada, April 12-16, 1992.

Nicholl, M.J., R.J. Glass, and H.A. Nguyen, Small-scale behavior of single gravity-driven fingers in an initially dry fracture, Proc. of the Fourth Ann. Int. Conf. on High Level Rad. Waste Mgmt., 2023-2032, Am. Nuclear Soc., Las Vegas, Nevada, April 26-30, 1993a.

Nicholl, M.J., R.J. Glass, and H.A. Nguyen, Wetting front instability in an initially wet unsaturated fracture, Proc. of the Fourth Ann. Int. Conf. on High Level Rad. Waste Mgmt., 2061-2070, Am. Nuclear Soc., Las Vegas, Nevada, April 26-30, 1993b.

Nicholl, M.J., R.J. Glass, and S.W. Wheatcraft, Gravity-Driven infiltration instability in initially dry nonhorizontal fractures, Water Resources Research, 30 (9), 2533-2546, 1994.

Nicholl, M.J., H. Rajaram, and R.J. Glass, Factors controlling satiated relative permeability in a partially-saturated horizontal fracture, Geophysical Research Letters, 27(3), 393-96, 2000.

Or, D., M. Tuller, R. Fedors, and R. Green, Hydraulic properties of partially saturated fractured porous media, Fall 1999 Meeting of the Am. Geophys. Union, San Francisco, CA, (H51E-02), EOS, 80(46), F458, 1999.

Peters, R.R., and E.A. Klavetter, A continuum model for water movement in an unsaturated fractured rock mass, Water Resources Research, 24(3), 416-430, 1988.

Pruess, K., and J.S.Y. Wang, Numerical modeling of isothermal and nonisothermal flow in unsaturated fractured rock - A review, Flow and Transport Through Unsaturated Fractured Rock, D.D. Evans and T.J. Nicholson, editors, Geophysical Monograph 42, Am. Geophys. Union, Washington, D.C., 11-22, 1987.

Renshaw, C.E., Influence of subcritical fracture growth on the connectivity of fracture networks, Water Resources Research, 32(6), 1519-1530, 1996.

Russell, C.E., J.W. Hess, and S.W. Tyler, Hydrogeologic investigation of flow in fractured tuffs, Rainier Mesa, Nevada Test Site, in Flow and Transport Through Unsaturated Fractured Rock, D.D. Evans and T.J. Nicholson, editors, Geophysical Monograph 42, Am. Geophysical Union, Washington DC, 43-50, 1987.

Su, G.W., J.T. Geller, K. Pruess, and F. Wen, Experimental studies of water seepage and intermittent flow in unsaturated, rough-walled fractures, Water Resources Research, 35(4), 1019-1037, 1999.

Throckmorton, C.K., and E.R. Verbeek, Joint networks in the Tiva Canyon and Topopah Springs tuffs of the Paintbrush Group, southwestern Nevada, USGS Open-File report 95-2, United States Geological Survey, Denver, Colorado, 1995.

Tokunaga, T.K. and J. Wan, Water film flow along fracture surfaces of porous rock, Water Resources Research, 33(6), 1287-1295, 1997.

Wang, J.S.Y., and T.N. Narasimhan, Hydrologic mechanisms governing fluid flow in a partially saturated, fractured, porous medium, Water Resources Research, 21(12), 1861-1874, 1985.

Wang, J.S.Y., and T.N. Narasimhan, Unsaturated flow in fractured porous media, in Flow and contaminant transport in fractured rock, Bear, J., C.f. Tsang, and G. de Marsily eds., Academic Press, San Diego, 560 pp., 1993.

Wilder, D.G., W. Lin, S.C. Blair, T. Buscheck, R.C. Carlson, K. Lee, A. Meile, A.L. Ramirez, J.L. Wagoner, and J. Wang, Large Block Test Status Report, UCRL-ID-128776, University of California, Lawrence Livermore National Laboratory, Livermore, California, 1997.

Yang, I.C., G.W. Rattray, and P. Yu, Interpretation of chemical and isotopic data from boreholes in the unsaturated zone at Yucca Mountain, Nevada, USGS Water-Resources Investigations Report 96-4058, 58 p., United States Geological Survey, Denver, Colorado, 1996.

Figure Captions

Figure 1: Sketch showing the general site layout with respect to other activities [after Lin et al., 1994]; drawing is not to scale. Our infiltration test was performed in the southwest corner of the region excavated to expose the LLNL Large Block. Fractures exposed on the pavement area, and in pits to the south and west of the excavation were mapped by the USGS [Throckmorton et al., 1995]. Yucca Mountain is located directly to the west, and 40 Mile Wash is to the east.

Figure 2: Fracture pavement maps for levels 0 through 11; areas in which tracer was observed are shown in gray. Level 0 is the infiltration surface, where mapping was limited to areas within the infiltration basin. At each level, the mapped region is outlined; estimates of tracer location outside that region are based on 35 mm slides and notes taken during the excavation process. The ERT array is shown as solid circles; the smaller circles shown at level 0 represent the surface electrodes, and numbers adjacent to the larger circles represent the string numbers (1-4) for the primary array. Also, the location of a persistent near vertical fracture trending NE-SW is marked with a black square.

Figure 3: Example pavement map collected ~3.1 m below the infiltration surface. Distribution of tracer is concentrated in the north and northwest portions of the mapped region. The extreme southwest corner remains untouched by the flow field, as it did throughout the excavated depth. The tracer pulse seems to be somewhat split, with the portion to the southeast being fragmented. Within this map, one can see a number of small scale flow features: (1) fragmented flow along a single fracture; (2) concentration of flow at fracture intersections; (3) bypassing of fractures, despite obvious physical connection to the flow field; and (4) flow on subhorizontal features.

Figure 4: Dip was measured for ~77% of the mapped fractures. Poles of the measured planes are plotted on a polar equal-area projection. Data is subdivided into three groups on the basis of measured trace length (0-1m, 1-2m, and >2m). Data shows at least two groups of steeply dipping, extensive (trace length > 2m) fractures. Measured orientation of the smaller fractures shows more scatter than that for the extensive features. Our data is consistent with USGS measurements at an adjacent site (TOB1) reported by Throckmorton et al. [1995].

Figure 5: Estimated extent of tracer at each level of the excavation (see figure 2); on average, pavements were separated vertically by ~0.5 m. Estimated extent of the flow field is seen to increase rapidly directly below the infiltration basin, oscillate near the larger value, and then contract significantly near the bottom of the excavation.

Figure 6:. Tracer on the surface of an extensive near-vertical fracture exposed in the excavation wall ~1 m south of the mapped region. The flow field contacted a limited portion of this surface, which belongs to a fracture that did not pass through the mapped prism. Connection to the infiltration surface appears to have occurred through the two near-vertical fractures penetrating into the excavation wall near the center of the photograph. Note the absence of tracer on a third near vertical fracture near the left edge of the photograph, and a sub-horizontal feature near the top.

Figure 7: View looking down on the mapped area at a depth of ~2.2 m below the infiltration surface. Tracer stain is clearly concentrated in the northwest corner of the mapped area (lower left corner of the grid) and extends outward in that direction. Photograph also shows tracer on a steeply dipping fracture exiting the mapped area in a

direction slightly north of east (left of the shovel). Buffer zone surrounding the LLNL Large Block can be seen in the upper left of the photograph.

Figure 8: Complicated flow structure within the plane of a single fracture; lens cap is shown for scale. Sample was found within the excavated rubble at a depth of ~3-4 m below the infiltration surface; however, the horizontal location is not known. Tracer appears to be connected in all directions, suggesting capillary dominated flow. Large portions of the aperture field were apparently bypassed, and trapped by the invading fluid.

Figure 9: Evidence of preferential flow along a fracture plane; lens cap is shown for scale. Sample was found within the excavated rubble at a depth of ~3-4 m below the infiltration surface; however, the horizontal location is not known. Flow structure spans the fracture in only one direction, suggestive of a gravity-driven finger.

Figure 10: Dark stain near the base of this near vertical fracture fades upwards; character of the stain suggests capillary rise.

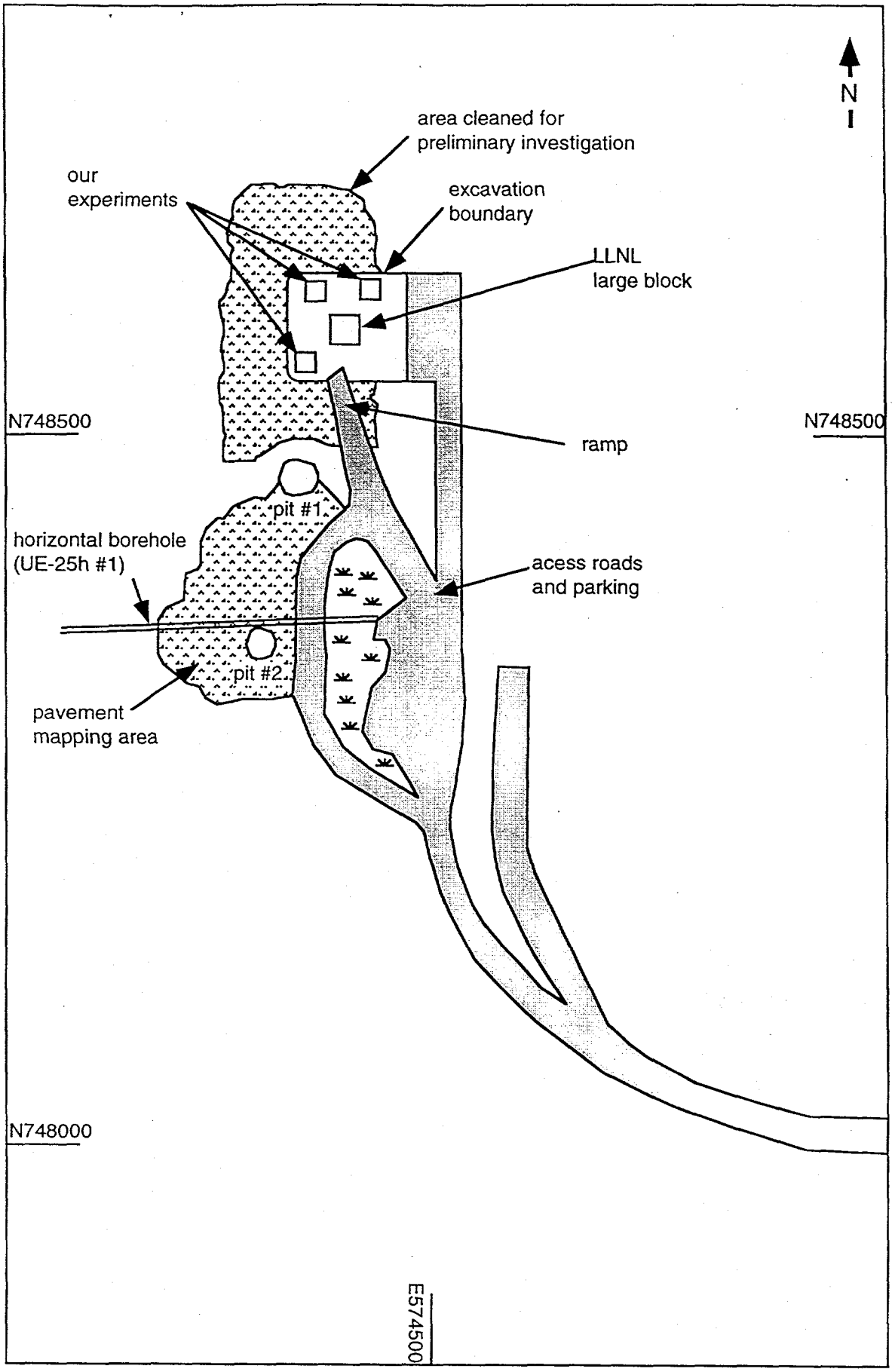

Figure 1 (Glass and Nicholl)

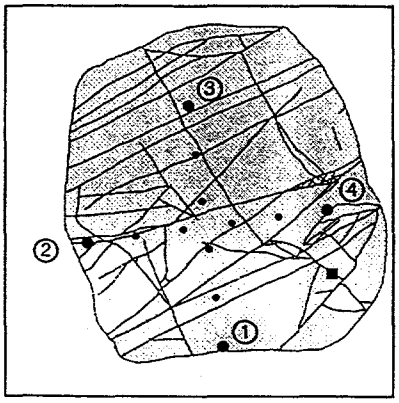

Figure 2 level 0 (Glass and Nicholl)

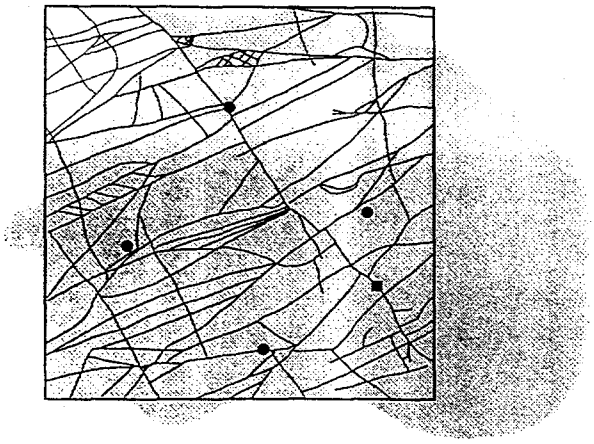

Figure 2 level 1 (Glass and Nicholl)

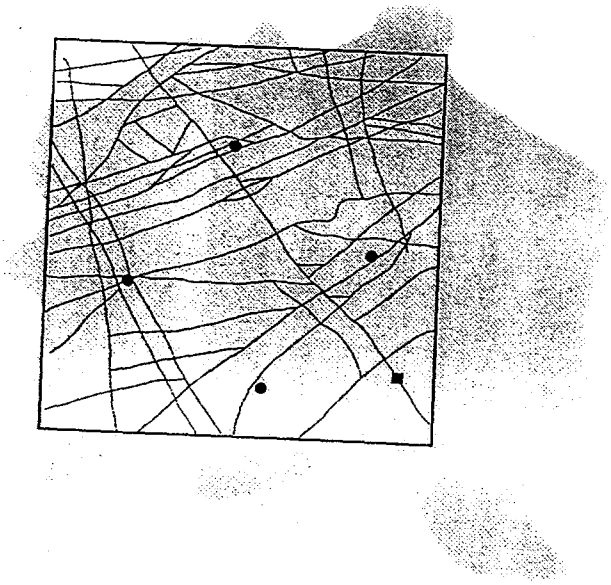

Figure 2 level 2 (Glass and Nicholl)

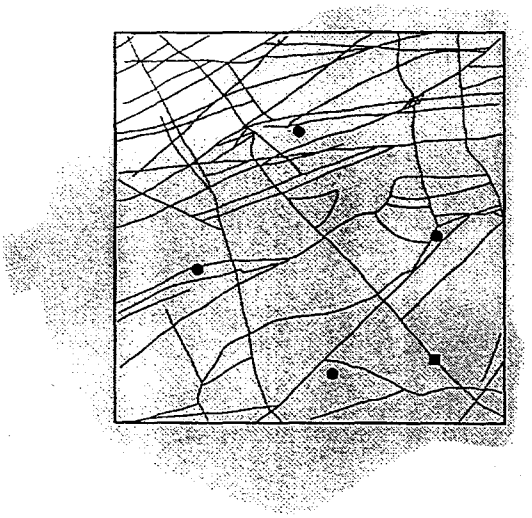

Figure 2 level 3 (Glass and Nicholl)

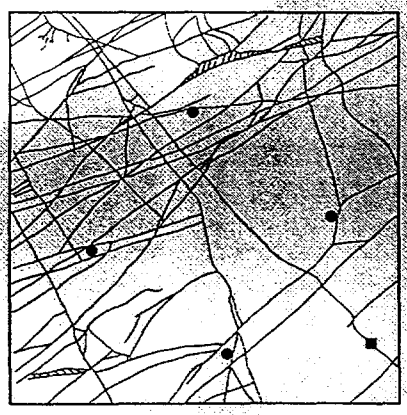

Figure 2 level 4 (Glass and Nicholl)

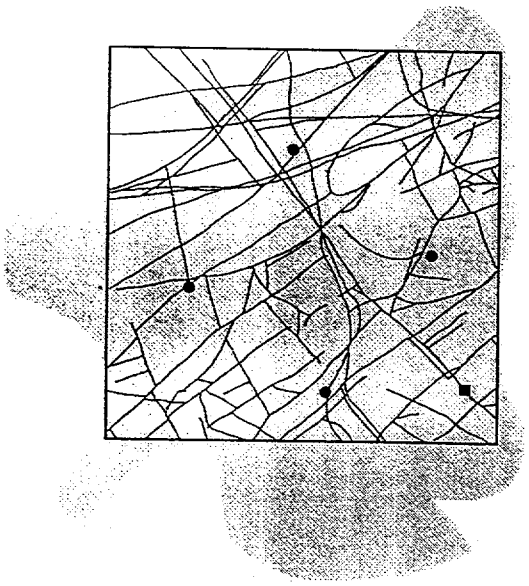

Figure 2 level 5 (Glass and Nicholl)

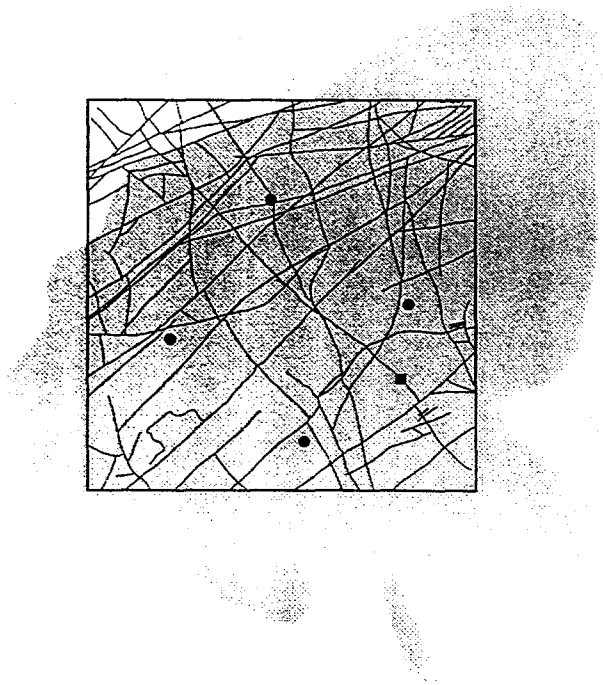

Figure 2 level 6 (Glass and Nicholl)

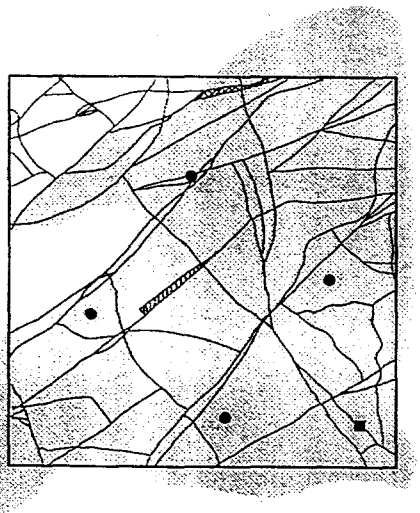

Figure 2 level 7 (Glass and Nicholl)

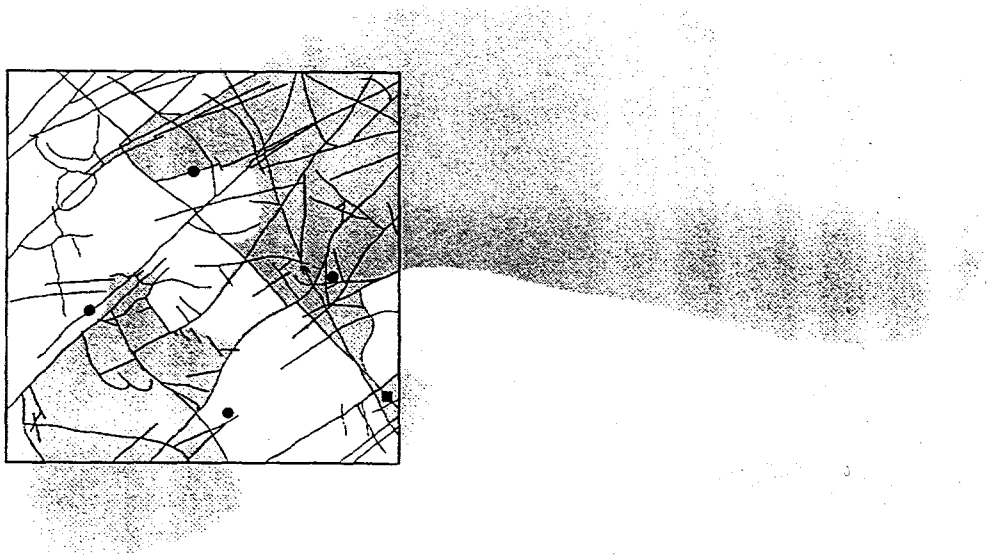

Figure 2 level 8 (Glass and Nicholl)

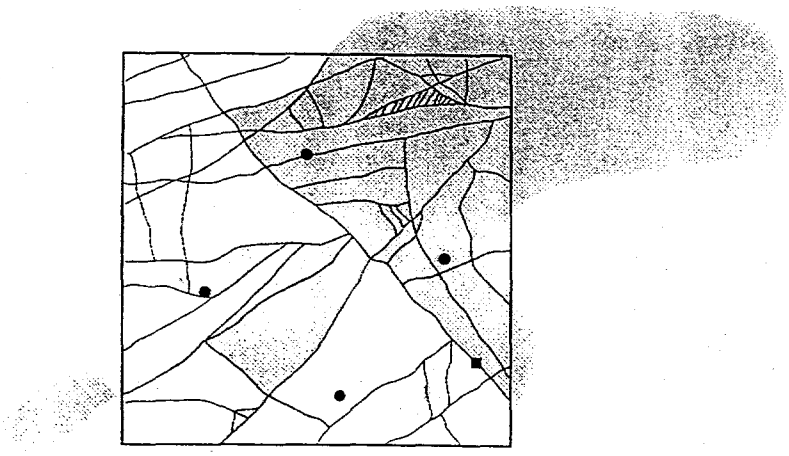

Figure 2 level 9 (Glass and Nicholl)

Figure 2 level 10 (Glass and Nicholl)

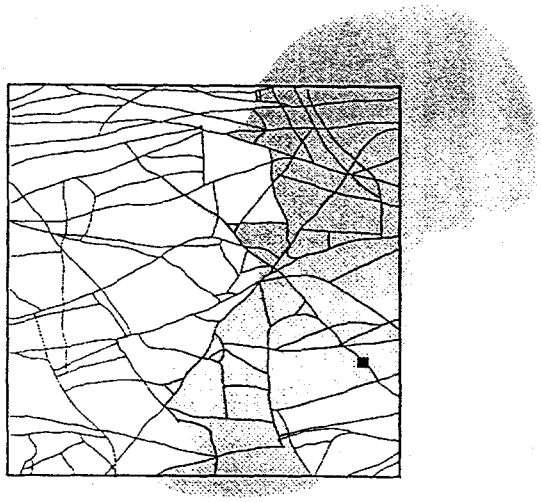

Figure 2 level 11 (Glass and Nicholl)

FIGURE 3 CLASS + NICHOLL

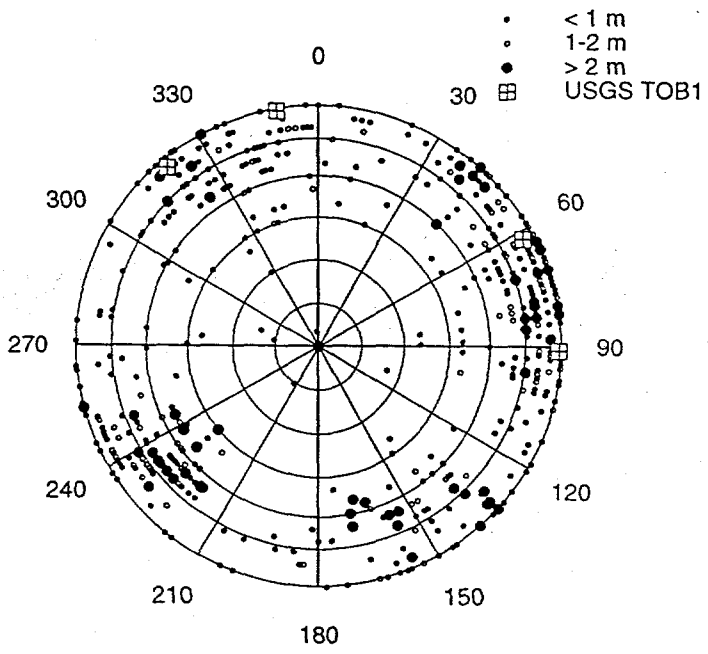

Figure 4 (Glass and Nicholl)

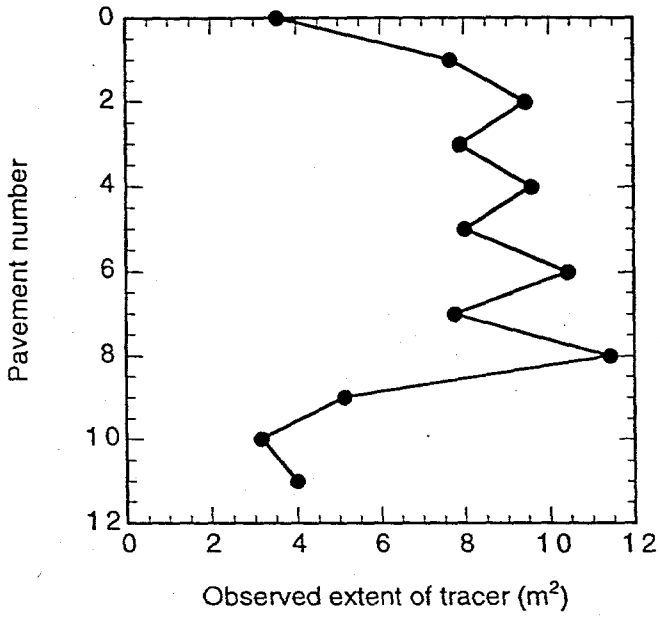

Figure 5 (Glass and Nicholl)

FIGURE 6

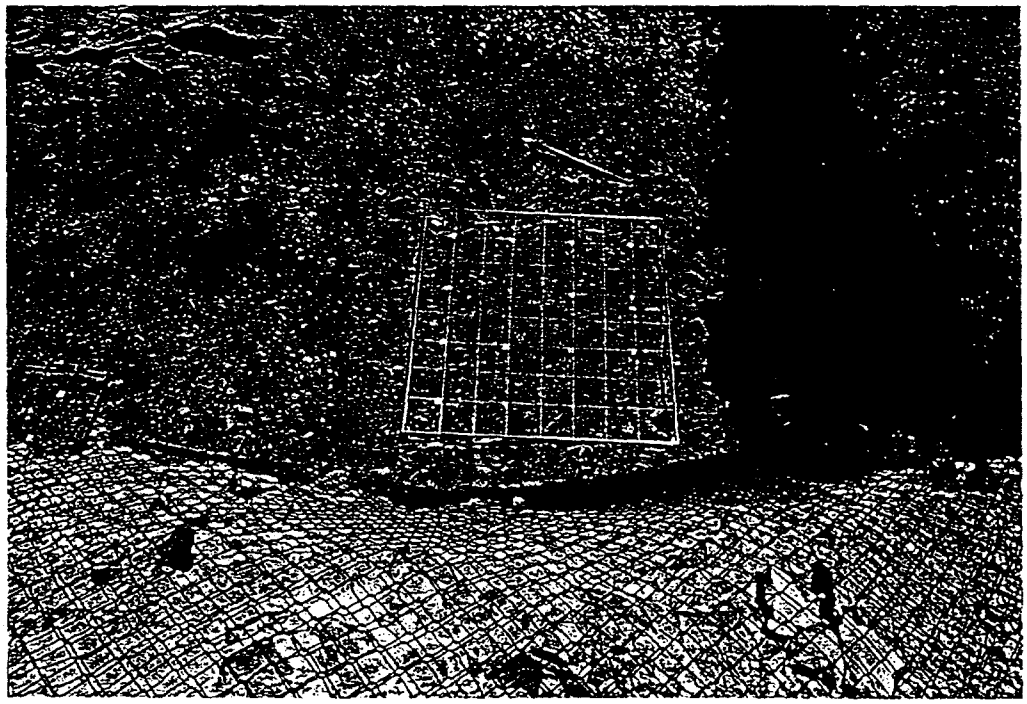

FIGURE 7

FIGURE 8

FIGURE 9

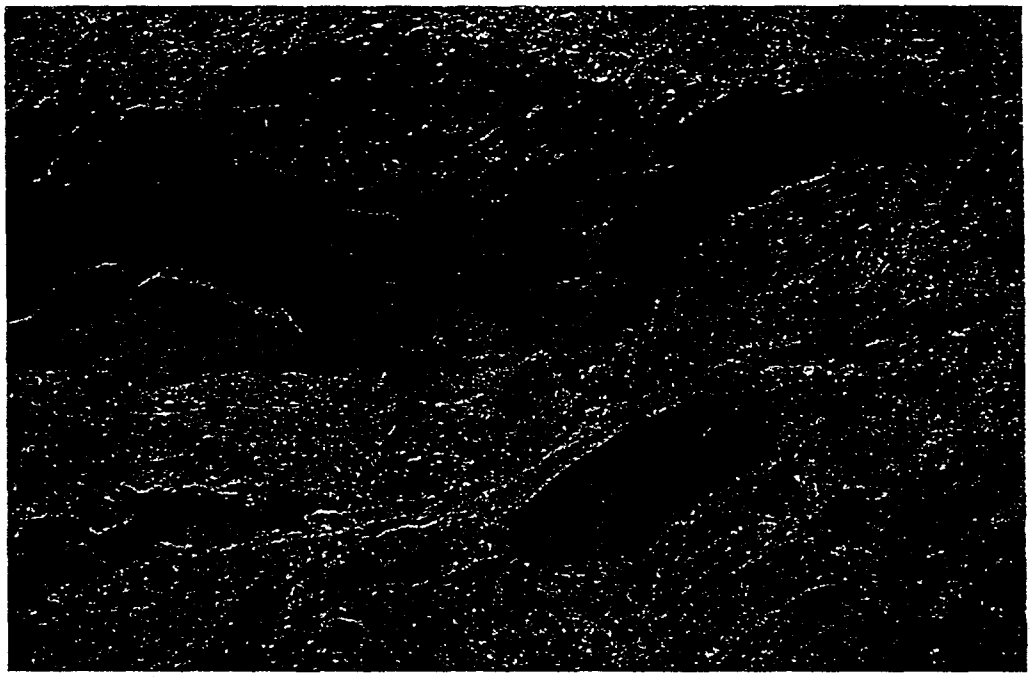

FIGURE 10